

A low-speed camera DIC approach for measuring synchronous vibrations in rotating disks

*Original*

A low-speed camera DIC approach for measuring synchronous vibrations in rotating disks / Occhipinti, S., Cesaretti, A., Firrone, C.M., Neri, P., Botto, D.. - In: MECHANICAL SYSTEMS AND SIGNAL PROCESSING. - ISSN 0888-3270. - ELETTRONICO. - 254:(2026). [10.1016/j.ymsp.2026.114351]

*Availability:*

This version is available at: 11583/3010693 since: 2026-05-09T07:28:50Z

*Publisher:*

Elsevier

*Published*

DOI:10.1016/j.ymsp.2026.114351

*Terms of use:*

This article is made available under terms and conditions as specified in the corresponding bibliographic description in the repository


*Publisher copyright*

(Article begins on next page)



Full length article

## A low-speed camera DIC approach for measuring synchronous vibrations in rotating disks

Serena Occhipinti <sup>a</sup>, Alessandra Cesaretti <sup>a</sup>, Christian M. FIRRONE <sup>a</sup>, Paolo Neri <sup>b</sup>,  
Daniele Botto <sup>a</sup>\*.

<sup>a</sup> Department of Mechanical and Aerospace Engineering, Politecnico di Torino, Corso Duca degli Abruzzi 24, Torino, 10129, Italy

<sup>b</sup> Department of Civil and Industrial Engineering, Università di Pisa, Largo L. Lazzarino 1, Pisa, 56122, Italy

### ARTICLE INFO

Communicated by P. Pennacchi

#### Keywords:

Vibrations  
Bladed disks  
Spinning test  
Optical technique  
DIC  
Downsampling

### ABSTRACT

During operation, turbomachinery blades are subjected to dynamic excitations, which are the primary drivers of high-cycle fatigue, the leading cause of failure in bladed disks. Therefore, accurate measurement of their dynamic response under resonance is critical for reliable design. Traditional contact-based measurement techniques suffer from drawbacks such as added mass, limited lifespan, and complex data transmission, prompting interest in non-contact alternatives. This paper explores the application of digital image correlation (DIC) for analyzing synchronous vibrations in bladed disks. The proposed approach employs low-speed, high-resolution cameras combined with downsampling strategies to enable cost-effective, full-field, high-resolution measurements. A signal processing technique, the circumferential harmonic fit (CHF), is proposed and applied to extract system parameters from downsampled displacement data. The methodology is applied on a simplified bladed disk mounted on a spinning rig, demonstrating successful identification of operational deflection shapes at resonance.

## 1. Introduction

### 1.1. Background and motivation

Bladed disks, sometimes referred to as blisks, are subject to variable loads in turbine or compressor stages. These loads can lead to forced vibration responses that may occur at or near a blade's natural frequencies. Synchronous blade response occurs when a blade's vibration frequency is an integer multiple of the engine rotation speed. Synchronous vibrations can result from mechanical effects, such as residual rotor imbalance, or aerodynamic effects, such as uneven pressure distribution within the airstream caused by the engine intake geometry, combustors and the wakes produced by the upstream stators. Vibration can lead to crack formation, which significantly reduces the fatigue life of blades. Therefore, measuring the dynamic behavior of these structures under resonant conditions is crucial for design purposes. A further complication arises from mistuning, i.e., unintentional deviations in disk geometry, material distribution, or boundary conditions. These break the cyclic symmetry of the system and can cause mode localization and frequency splitting, leading to a significant change in vibration response [1]. Because mistuning is highly sensitive to manufacturing, it is difficult to accurately predict by using numerical simulations alone. Therefore, experimental testing remains essential to assess mistuning effects and to validate or calibrate mistuning models used in design. An extensive review of the

\* Corresponding author.

E-mail addresses: [serena.occhipinti@polito.it](mailto:serena.occhipinti@polito.it) (S. Occhipinti), [alessandra.cesaretti@polito.it](mailto:alessandra.cesaretti@polito.it) (A. Cesaretti), [christian.firrone@polito.it](mailto:christian.firrone@polito.it) (C.M. FIRRONE), [paolo.neri@unipi.it](mailto:paolo.neri@unipi.it) (P. Neri), [daniele.botto@polito.it](mailto:daniele.botto@polito.it) (D. Botto).

<https://doi.org/10.1016/j.ymssp.2026.114351>

Received 29 October 2025; Received in revised form 28 March 2026; Accepted 26 April 2026

Available online 4 May 2026

0888-3270/© 2026 The Authors. Published by Elsevier Ltd. This is an open access article under the CC BY license (<http://creativecommons.org/licenses/by/4.0/>).

literature on mistuning is provided in [2]. This paper focuses on the prediction and understanding of the forced response of mistuned bladed disks, with particular emphasis on mitigating the harmful effects of mistuning on blade vibration and the associated stresses. Reduced-order modeling and simulation are also discussed in this paper. A reduced-order model with variable speed together with a mistuning identification method is proposed in [3].

Traditionally, strain gauges have been the most reliable method of monitoring vibrations of the rotor blade [4]. However, they require complex wireless systems or slip rings to transmit data, and their added mass and stiffness can alter the dynamic behavior of the system. In addition, strain gauges offer limited service life and provide data only at localized points.

In this context, non-contact measurement techniques are gaining interest. Blade tip timing (BTT) has emerged as a valid alternative [5]. BTT relies on optical probes mounted on the engine casing to record the time instants at which each blade tip passes in front of the probes. By comparing these measured arrival times with the expected timings assuming rigid-body motion, the vibration of the blades can be measured. The effective sampling frequency of BTT is determined by both the number of probes and the rotational speed of the disk. In cases where the blade response signal is downsampled, that is, when the sampling frequency is below the Nyquist–Shannon limit, specialized identification techniques must be employed to estimate the modal parameters of the blade. These techniques can be categorized as indirect or direct methods. Indirect methods require data from one or two probes, while the disk rotation speed varies in such a way that the frequency of the excitation sweeps a range of frequencies around its natural frequency. A well-known example of such an approach is the Single Parameter Method [6], which estimates modal parameters by fitting experimental data to the response of a single degree of freedom (SDOF) vibrating system. Several extensions have been proposed to account for more complex dynamic behaviors. For instance, the multi degree of freedom method [7] allows the identification of modal parameters in mistuned rotating blades and an improved SDOF-based identification model [8] that incorporates the transient response of the system, enables a more accurate estimation of dynamic parameters when the blade crosses resonance rapidly.

Direct methods use data recorded by a number of probes (typically four) over a limited number of revolutions at a nominally constant rotation speed. These methods usually perform a least-squares sine fit of the probe data. Circumferential Fourier Fit [9] is one of the most common direct methods used for parameter identification. The method is based on a fitting procedure applied at each rotational speed to identify the vibration amplitude and phase of each blade.

While BTT sensors are typically oriented radially inward, alternative configurations have been explored to capture different displacement components [10]. However, BTT remains inherently one-dimensional and limited to asynchronous measurement at specific points, usually the blade tips.

Another promising non-contact approach for measuring vibrations of rotating structures makes use of a scanning laser Doppler vibrometer (SLDV) combined with an optical derotator. The derotator synchronizes the laser with the disk's rotation, effectively making the laser beam following measurement points during rotation [11]. In [12] the laser beam was continuously swept on a rotating fan blade, whose position was detected by real time processing of images captured by a camera. These systems enable non-invasive, high-temporal-resolution vibration measurements at specific points. Despite its precision, the high cost and complexity of such systems is a drawback. In [13], a custom-built derotator was used with an SLDV for fan vibration analysis. Similarly, [14] proposed a method using a system of plane mirrors to track rotating points. However these approaches also relies on complex hardware sensitive to misalignment and as BTT only captures one-dimensional displacements at a limited number of points.

More recently, digital image correlation (DIC) has shown potential for rotor vibration analysis. DIC can track points on the surface of a structure, enabling its full-field 3D displacement measurements. While well established for non-rotating structures, applying DIC to rotating systems is challenging. Traditional DIC algorithms struggle with large rigid-body displacements and rapid changes in the field of view, which can lead to decorrelation—a failure to track points across image frames. To mitigate this issue, incremental DIC is commonly employed. In this approach, the reference image is updated periodically when the angular displacement exceeds the trackable limit, typically less than 10 degrees for standard DIC algorithms, thereby avoiding decorrelation through images sequence. Incremental DIC was used for experimental modal analysis of a rotating tire [15] and of a disk [16]. However, each reference update introduces error [17], and in rotating systems where rigid-body motion causes large rotation and displacement, frequent updates result in noise accumulation. This is the reason why researchers are proposing new DIC algorithms that account for large rotation angles solving decorrelation problem of traditional ones [18,19].

High-speed cameras are often used for DIC measurements because their kHz-range frame rates make them ideal for capturing high-frequency modes. However, these cameras have significant drawbacks: their high cost often makes them inaccessible for many research institutions, and they generally offer lower spatial resolution than standard low-speed industrial cameras, limiting the achievable DIC sensitivity. To overcome these limitations, recent advancements have enabled the use of low-speed cameras for dynamic measurements (low-speed DIC) of non-rotating structures. It has been done by recording motion at frequencies beyond the Nyquist–Shannon limit and processing them with downsampling techniques. For example, in [20] it was demonstrated the use of low-speed DIC to measure turbine blade vibration frequencies up to 6.5 kHz with micrometer sensitivity by employing mono-harmonic excitation. Similarly, Kato et al. [21] showed that images captured at 10 fps could measure vibration modes of beams oscillating at single frequencies ranging from 170 Hz to 3210 Hz using compressive sensing (CS) [22]. CS exploits the sparsity of periodic signals in the Fourier domain to reconstruct the signal. Other researchers have extended these methods to capture more complex dynamics. For instance, in [23] nonlinear vibrations of a beam excited by a single harmonic force were measured by low-speed DIC. To avoid aliasing, harmonics were fitted to the experimentally measured response frequencies, which were determined as submultiples and multiples of the excitation frequency. Although downsampling-based methods generally cannot capture the entire spectrum, the work presented in [24] employed low-speed cameras to randomly downsample a beam's impulse response and reconstructed the frequency response function (FRF) by fitting modal parameters to an impulse response model.

## 1.2. Objective

This paper investigates the application of DIC using low-speed cameras combined with downsampling techniques for full-field, high-frequency synchronous vibration analysis of a rotating blisk. The proposed methodology was designed to address the two primary limitations of DIC in rotor applications: decorrelation resulting from large rigid displacements induced by rigid rotation, and the requirement of high-speed cameras. By capturing one image per revolution at a fixed angular reference position, the approach avoids decorrelation errors and allows the use of standard DIC software. Moreover, this strategy allows the use of low-cost, high-resolution industrial cameras, offering a cost-effective alternative to high-speed cameras, with improved spatial resolution analysis.

A novel identification technique called circumferential harmonic fit is introduced to enable analysis of rotating modes of blisk despite sampling below the Nyquist–Shannon limit. The methodology was experimentally validated on a simplified blisk, the dummy blisk, mounted on a custom spinning test rig. First, the dynamic behavior of the dummy blisk was predicted via finite element analysis (FEA) and then it was validated through SLDV measurements in a non-rotating condition.

This paper is organized as follows. Section 2 provides an overview of the main steps in the proposed procedure. It describes the relationship between engine order and nodal diameter when exciting rotating disks. Furthermore, this section thoroughly explains the proposed method, called the circumferential harmonic fit, which is used to derive modal information from downsampled data of rotating disks. The subject of Section 3 is the description of the experimental setup. This section provides details on the test article, the permanent magnet excitation system, and the digital image correlation system that were used for this experiment. The preparatory analyses conducted prior to the rotation tests, the finite element analysis, and the hammer test are described in Section 4. This section presents the experimental and numerical modal analysis, as well as the Campbell diagram of the test article. Finally, Section 5 summarizes the primary outcomes of the activity in terms of resonance frequencies and modal shapes. The main conclusions are drawn in Section 6.

*Notation and convention:* Throughout this paper,  $f$  and  $\omega$  denote frequency, expressed in Hz and rad/s, respectively.  $\Omega$  is used for rotational speed in rpm.

## 2. Methodology

The proposed methodology enables analysis of the dynamics of a rotating blisk using DIC with low-speed, high-resolution cameras. Two synchronized cameras capture one image per revolution of a blisk as it rotates on a spin rig. The blisk undergoes a controlled acceleration with a linearly increasing rotational speed, while being excited by a train of impulses whose frequency is proportional to the rotational speed. The measurement process involves the following key steps:

- **Surface preparation:** To ensure accurate DIC analysis, each set of pixels (subsets) representing a point on the blisk's surface must be unique. Typically, when the surface does not naturally meet this requirement, a black and white random pattern (speckle pattern) is painted or sprayed to the surface to enhance measurement accuracy and precision. Guidelines on traditional speckle pattern generation techniques can be found in [25], while a noninvasive solution using laser light to generate speckle patterns without modifying the surface of the specimen is proposed in [26].
- **Excitation:** The blisk is excited by a train of impulses with a frequency dependent on its rotation speed. In particular, excitation is designed to have a frequency that is an integer multiple of the rotation speed, resulting in a sweep excitation as the speed increases linearly.
- **Images acquisition and DIC:** Two cameras capture an image during each revolution, with the image always taken at the same arbitrarily chosen angle of rotation. An external optical probe triggers the cameras by sending a pulse signal to both whenever the blisk reaches this angle. These images are processed using DIC to compute the three-dimensional, full-field displacement of the blisk's surface at the time in which the blisk passes from the reference position. This sampling strategy results in a downsampling of blisk vibrations.
- **Data post-processing:** Since displacement signals computed by DIC are downsampled, a dedicated identification algorithm, the Circumferential Harmonic Fit (CHF), is proposed to extract modal information.

### 2.1. Excitation of rotating systems

In rotating systems, excitations are often characterized by a frequency  $f$  which is proportional to the angular velocity  $\Omega$ :

$$f = \frac{EO \cdot \Omega}{60} \quad (1)$$

In simple terms,  $EO$  in Eq. (1) is the engine order, i.e., a dimensionless value that indicates how often an excitation repeats for each revolution. For example, if the disk of a turbine is excited by the wakes of the upstream stator vanes, then one  $EO$  corresponds to the number of stator vanes. Such excitations typically lead to synchronous vibrations, where the excitation frequency is an integer multiple of the angular velocity.

Resonance occurs when the excitation frequency matches a natural frequency  $\omega_n$  of the blisk and the  $EO$  coincides with the associated harmonic index,  $h_n$ . The harmonic index is closely related to the nodal diameter ( $ND$ ), a non-negative integer that gives a visual representation of the number of zero displacement lines passing through the center of the blisk. For a blisk with  $N$  sectors,

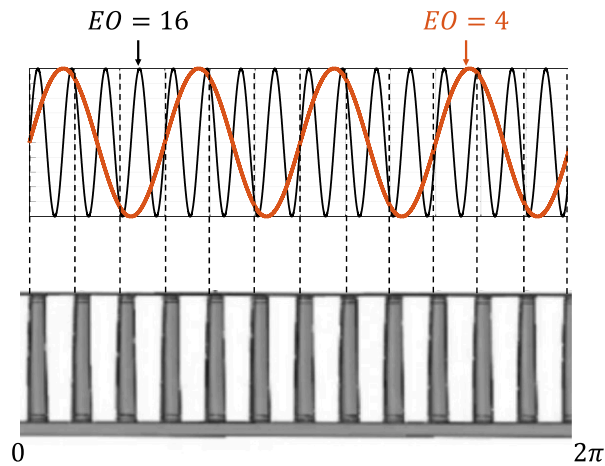


**Fig. 1.** Discretization of an  $EO = 16$  excitation by a blisk with  $N = 12$  blades. In this case, the blisk responds as if excited at  $EO = 4$  ( $z = 1$ ).

which usually corresponds to the number of blades, the number of possible nodal diameters ranges from 0 to  $N/2$  if  $N$  is even, and from 0 to  $(N - 1)/2$  if  $N$  is odd. The reader unfamiliar with periodic structures can find a comprehensive analysis of their behavior in [27].

An engine order  $EO$  is capable of exciting more nodal diameters  $ND$  if the following condition is met:

$$EO = z \cdot N \pm ND \quad \forall z \in \mathbb{N} \quad (2)$$

where  $z$  is a positive integer. Eq. (2) shows that resonance occurs when the spatial distribution of the excitation force matches the modal shape of the structure ( $z = 0, EO = ND$ ), or when the structure experiences an equivalent distribution because of spatial aliasing effects ( $z \neq 0, EO \neq ND$ ), provided that the excitation frequency is close to the natural frequency associated to that nodal diameter. In the latter case, the rotating excitation force is downsampled by the discrete number of blades, causing the blisk to respond as though it were subjected to an excitation with  $EO = ND$ . Appendix provides a detailed explanation of this phenomenon, illustrated in Fig. 1.

In this work, the blisk is excited by a periodic train of impulses while undergoing constant acceleration, resulting in a linear increase in rotational speed. Specifically, each blade receives an impulse as it passes through predefined angular positions, producing a sweep excitation whose frequency increases linearly and is proportional to the rotational speed. According to Eq. (2), the number of pulses per revolution  $EO$  is chosen to excite a mode shape characterized by the specific nodal diameter under consideration.

## 2.2. Images acquisition and DIC

DIC is a camera-based technique used to measure full-field displacement on the surface of a structure. It operates by analyzing a series of images of a specimen undergoing deformation, tracking the motion of pixel subsets from a reference image to subsequent deformed images. When performed with a single camera, DIC enables two-dimensional displacement analysis. Using two synchronized cameras to capture images from different viewpoints, 3D-DIC, allows for three-dimensional motion tracking. 3D-DIC consists of three main stages: cameras calibration, 2D-DIC images processing, and triangulation.

*Calibration* defines the intrinsic and extrinsic parameters of each camera using a geometric model that relates image points on the sensor to corresponding 3D locations in space [28]. In this study, camera calibration was carried out using MATLAB's Stereo Camera Calibrator App [29].

The *2D-DIC* algorithm processes images from each camera to track the position of pixel regions (subsets). For this purpose, the open-source software Ncorr [30] has been used in this work. Ncorr employs a subset-based approach, where each measurement point corresponds to a circular subset in the reference image. The displacement is determined by mapping each subset to its deformed counterpart via a transformation function. In Ncorr, this transformation is limited to a first-order linear model, allowing for translation, shear, and normal deformation. The algorithm iteratively refines these parameters to maximize the correlation between subsets in the reference and deformed images.

Finally, *triangulation* is used to reconstruct the 3D positions of the tracked points by combining the 2D-DIC results from both cameras with the previously determined calibration parameters. This process yields accurate 3D displacement fields for each time frame.

One of the main challenges of applying DIC to measurements of rotating systems is the *decorrelation* caused by wide-angle rotation. Conventional 2D-DIC algorithms assume small angular differences between the reference and deformed subsets. When the rotation between consecutive images exceeds approximately 7 degrees, the initial estimate for the subset transformation becomes unreliable, often leading to failure in the correlation process.

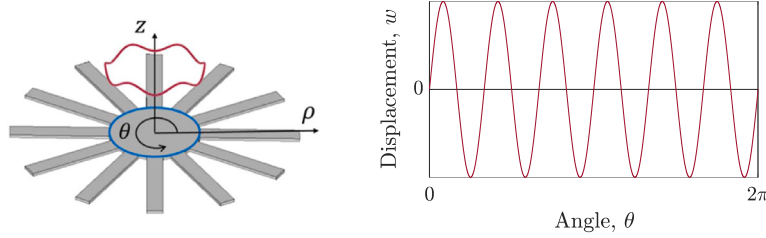


Fig. 2. Mode shape with ND = 6 (in red) plotted along the line denoted by the blue circumference in the left image. It appears as a sinusoidal wave, as shown in the right plot.

This study proposes an approach that overcomes this limitation: imaging is performed only when the rotating blisk is in the same predefined angular position. This sampling strategy eliminates the problems of decorrelation caused by large in-plane rotations, enabling reliable DIC tracking. However, this approach is limited in terms of temporal resolution. Specifically, the image sampling frequency  $f_s$  is equal to the rotational frequency which is given by

$$f_s = \frac{\Omega}{60} \tag{3}$$

Therefore, the synchronous excitation frequency  $f_v$  defined in Eq. (1) is related to the sampling frequency as follows

$$f_v = EO \cdot f_s \tag{4}$$

Consequently, the sampling frequency is lower than the actual vibration frequency (equal only when  $EO = 1$ ), so it does not satisfy the Nyquist–Shannon sampling theorem ( $f_s \leq 2f_v$ ). As a result, aliasing occurs, effectively downsampling the measured vibration signals. To correctly interpret these aliased signals, dedicated post-processing algorithms are required.

Despite this limitation, the sampling strategy offers a key advantage: it significantly reduces the required camera frame rate compared to conventional high-speed imaging, making it compatible with low-speed cameras and enabling high-resolution, low-cost measurement.

### 2.3. Displacement signal post-processing

To derive meaningful modal information from the downsampled DIC data and prevent aliasing errors, measurements are post-processed using a method called **circumferential harmonic fit (CHF)**. This method is conceptually aligned with the circumferential Fourier fit (CFF) technique [31,32], which is widely used in blade tip timing (BTT) analysis. In this work, however, the CFF was formulated in a novel way for application to DIC-based, full-field vibration measurements.

CHF assumes that, for a given excitation frequency  $f$  defined in Eq. (1), the operational deflection shape (ODS) – associated with the synchronous response of the structure and obtained by selecting homologous points on its surface – can be represented as a harmonic spatial wave (see Fig. 2). In a cylindrical coordinate system, where the axial axis aligns with the axis of symmetry, homologous points are defined as those sharing the same radial ( $\rho$ ) and axial ( $z$ ) coordinates. The harmonic wave describing the ODS has a spatial frequency equal to the number of nodal diameters characterizing the mode shape. This harmonic approximation is valid under the assumption that a single mode dominates the structural response and that the level of mistuning is sufficiently small so as not to completely destroy the cyclic symmetry of the blisk (small mistuning).

Accordingly, the displacement  $w$  as a function of angular position  $\theta$  and excitation frequency  $f$  can be written as:

$$w_{(\theta,f)} = c_{(f)} + Z_{(f)} \sin (ND \cdot \theta - \phi_{(f)}) \tag{5}$$

where:

- $c_{(f)}$  is the static displacement. Although  $c$  is theoretically independent of frequency, it is treated here as a function of  $f$  to account for practical variations in excitation force with vibration frequency,
- $Z_{(f)}$  is the frequency-dependent response amplitude,
- $\phi_{(f)}$  is the frequency-dependent phase delay.

Eq. (5) is derived under the assumption of a linear cyclic-symmetric response of the disk when subjected to synchronous excitation. If nonlinear effects become significant, they will manifest as additional harmonic components and the response can be calculated as shown in [23]. Eq. (5) can be rewritten as:

$$z_{(\theta,f)} = c_{(f)} + A_{(f)} \sin (ND \cdot \theta) + B_{(f)} \cos (ND \cdot \theta) \tag{6}$$

where  $A_{(f)} = Z_{(f)} \cos(\phi_{(f)})$  and  $B_{(f)} = Z_{(f)} \sin(\phi_{(f)})$ .

Given displacement measurements at  $N$  homologous angular positions  $\theta_i$  (with  $i = 1, 2, \dots, N$ ), the best-fit values of  $c_{(f^*)}$ ,  $A_{(f^*)}$  and  $B_{(f^*)}$  for a particular excitation frequency  $f^*$  can be estimated by solving the overdetermined system:

$$\begin{Bmatrix} w(\theta_1, f^*) \\ w(\theta_2, f^*) \\ \vdots \\ w(\theta_i, f^*) \\ \vdots \\ w(\theta_N, f^*) \end{Bmatrix} = \begin{bmatrix} 1 & \sin(ND \cdot \theta_1) & \cos(ND \cdot \theta_1) \\ 1 & \sin(ND \cdot \theta_2) & \cos(ND \cdot \theta_2) \\ \vdots & \vdots & \vdots \\ 1 & \sin(ND \cdot \theta_i) & \cos(ND \cdot \theta_i) \\ \vdots & \vdots & \vdots \\ 1 & \sin(ND \cdot \theta_N) & \cos(ND \cdot \theta_N) \end{bmatrix} \begin{Bmatrix} c(f^*) \\ A(f^*) \\ B(f^*) \end{Bmatrix} \quad (7)$$

$$w_{(\theta, f^*)} = \mathbf{M} \begin{Bmatrix} c(f^*) \\ A(f^*) \\ B(f^*) \end{Bmatrix}$$

where  $\mathbf{M}$  is a matrix containing the sinusoidal basis functions evaluated at each  $\theta_i$ . A least-squares solution provides the optimal parameters minimizing the residual between measured and fitted data. If the number of nodal diameters  $ND$  is not prior known, it can be identified iteratively by selecting the value that minimizes the residual of a least squares fit, or alternatively, by performing a Discrete Fourier Transform in the spatial domain of the experimental data. Once  $A_{(f)}$  and  $B_{(f)}$  are computed for each measured excitation frequency  $f$ , the vibration amplitude and phase delay are given by:

$$Z_{(f)} = \sqrt{A_{(f)}^2 + B_{(f)}^2}$$

$$\tan(\phi_{(f)}) = -\frac{B_{(f)}}{A_{(f)}} \quad (8)$$

Since the mode is rotating, the evolution of the amplitude,  $Z_{(f)}$ , and phase,  $\phi_{(f)}$ , as functions of the excitation frequency allows for the identification of resonance frequencies. Resonances can be detected by the characteristic  $90^\circ$  phase shift, provided that the frequency sweep starts sufficiently far from resonance, so that the initial deflection shapes are approximately in phase with the excitation. Additionally, if the excitation amplitude remains constant throughout the frequency sweep, resonance frequencies can be identified by peaks in the amplitude response  $Z_{(f)}$ .

The CHF method did not account for variations in response amplitude caused by asynchronous components arising after resonance crossing. Nevertheless, advanced identification techniques can address such contributions. For example, the work presented in [8] fits experimental data using a single degree of freedom model that incorporates transient effects, while in [33] wavelet transforms were used to isolate asynchronous dynamics and extract modal parameters.

### 3. Test rig

The methodology proposed in Section 2.3 was tested on a blisk with a simplified flat geometry, hereafter referred to as the dummy blisk. Made of aluminum, the dummy blisk has an outer diameter of 400 mm and consists of  $N = 12$  blades. Each blade is shaped like a cantilever beam, measuring 150 mm in length, 25 mm in width, and 5 mm in thickness. Although the test article features a simplified geometry, the concepts and algorithms developed in this work are general and can be readily extended to more complex disks.

The dummy blisk was mounted in a laboratory spinning rig with a vertical axis, where the electric motor is located below the blisk. This architecture enables the two cameras to fully frame the blisk. As shown in Fig. 3, the dummy blisk is clamped by a flange at the upper end of the shaft.

#### 3.1. Excitation system

The excitation system is sketched in Fig. 4. It consists of cylindrical permanent magnets that are fixed to the ground and interact with the rotating permanent magnets that are incorporated into the blisk. There is one magnet for each blade. The number of fixed magnets determines the engine order  $EO$ . This interaction results in a periodic train of force impulses at a fundamental frequency corresponding to the engine order, which increased linearly as the blisk's rotational speed. The polarity of the magnets was chosen so that the force would be repulsive, and this choice was based on the understanding that an attractive force could increase the risk of contact between magnets if the blade tip undergoes significant deformation. The permanent magnets (1) are mounted in the housing at the tip of a threaded rod (2) with an interference fit and glue. The threaded rod is screwed in a support (3). A bolt (4) locks the rod in place so that the permanent magnet (1) is at the desired height. This height defines the distance, the gap, between the fixed and permanent magnets, which regulates the magnitude of the magnetic force. The magnitude of the magnetic repulsion force is inversely proportional to the square of the gap. In the current tests, the gap was approximately 20 mm.

The support (3) is clamped between two coaxial rings. A lower ring (5) is bolted to the ground, and an upper ring (6) is bolted to the lower ring. A graduation is marked on the upper ring so that each support can be located at the desired angle. The permanent magnets were mounted at equally spaced angular positions. Four rods have been split in half, (7) and (8), so that a piezoelectric load cell (9) can be inserted below the fixed permanent magnet, allowing the excitation force to be measured.

One drawback of the proposed excitation system, based on permanent magnets, is the variability of the excitation force during testing. This is due to changes in the gap between the fixed and rotating magnets as the blisk vibrates. The magnetic force is

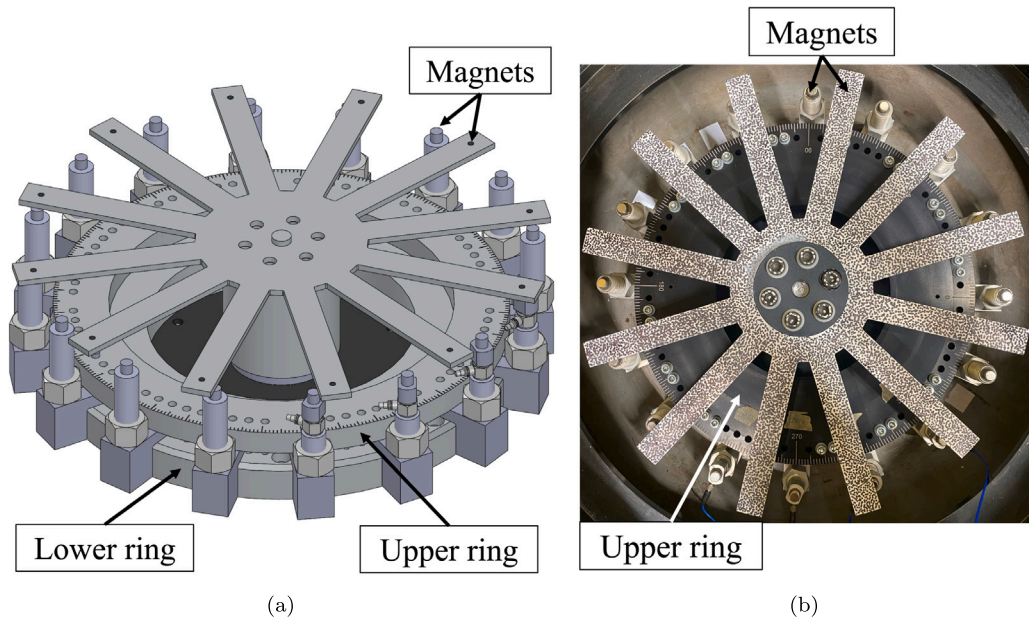


Fig. 3. (a) Sketch and (b) picture of the spinning rig.

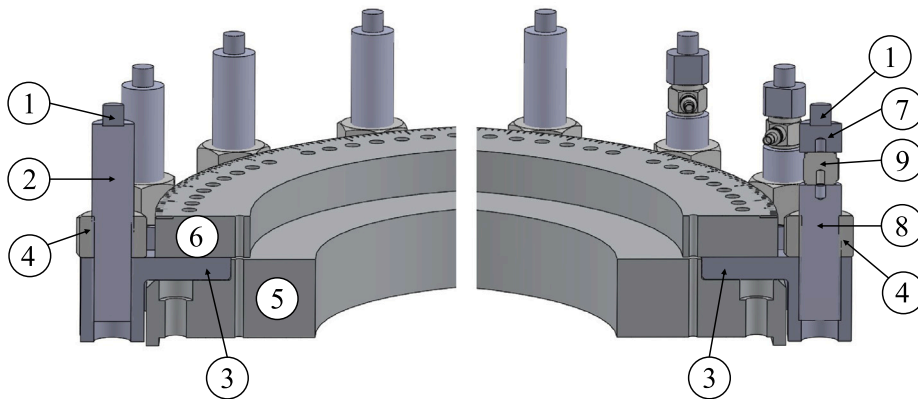


Fig. 4. Details of the excitation system with permanent magnets.

inversely proportional to the square of this gap. Increasing the initial gap would reduce the vibration amplitude, which would minimize fluctuations in the gap and excitation force. However, with the current setup, positioning the magnets farther from the blisk was not possible because the gap was already at its maximum. This issue is less significant in stiffer, more realistic blisks, where vibration amplitudes, and thus gap fluctuations, are smaller.

The blisk was excited with an engine order of sixteen,  $EO = 16$ . According to Eq. (2), this  $EO$  excites the mode shapes with nodal a diameter of four,  $ND = 4$ , when the excitation frequency is close to the natural frequency of these modes. The results of both the hammer test and the finite element analysis, as presented in Section 4, indicate that the first modal family with  $ND = 4$  occurs near 150 Hz. According to the blisk's Campbell diagram, see Fig. 6, this resonance condition is expected to occur at rotational speeds below 600 rpm. Therefore, a linearly increasing speed profile was implemented, ramping the blisk from 0 to 600 rpm over a duration of 11 min.

### 3.2. DIC system

The DIC system employed two Optomotive Spinosaurus cameras, each equipped with a 23 MP Fujinon lens featuring a 12 mm focal length. These cameras were mounted above the blisk using a rigid aluminum support frame, as shown in Fig. 5(a). To avoid motion blur during image capture of the rotating blisk, a short shutter time of 5  $\mu$ s was used. Due to the limited light, associated with

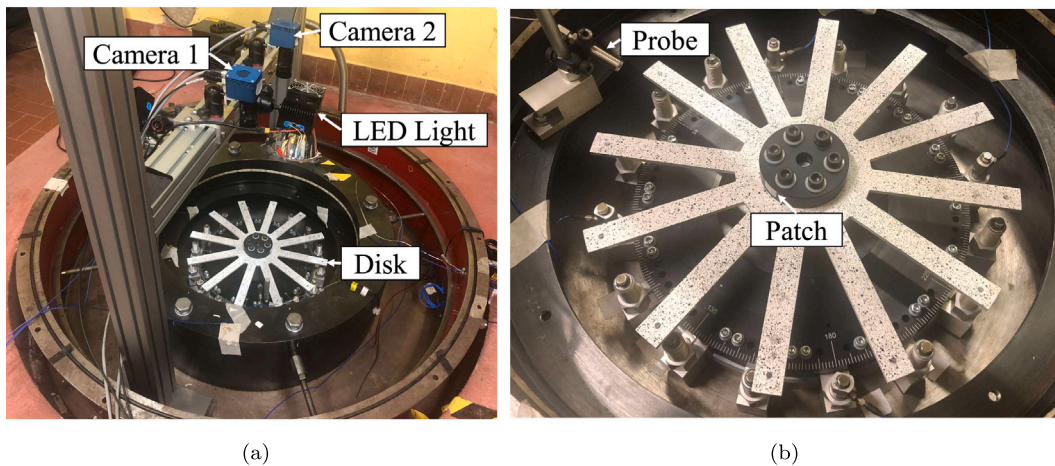


Fig. 5. (a) DIC cameras setup and (b) close-up view of the dummy blisk and probe that triggers cameras.

such a short shutter duration, additional high-intensity illumination was necessary to achieve sufficient image quality. Two 200 W LED lights were used, verified to provide uniform and bright illumination across the entire surface of the blade. This requirement is facilitated by the imaging strategy adopted, in which a single image is captured for each revolution. Under these conditions, the disk appears stationary from the camera's perspective, which greatly reduces sensitivity to uneven lighting or shadows. In contrast, when images are taken at varying angular positions, differences in illumination and reflections can introduce decorrelation and reduce measurement accuracy. In the present setup, the camera arrangement and field of view were selected to limit extreme viewing angles in the region of interest, ensuring that the angle between the viewing direction and surface normal remains within a range commonly considered acceptable for accurate correlation. Image acquisition was synchronized between the two cameras via a common TTL trigger signal. To ensure that an image was acquired at a consistent angular reference position on the blisk, an optical probe was mounted on the stationary rig structure and aligned with the upper flange of the rotating blisk, as shown in Fig. 5(b). A reflective tape patch was attached to the flange. Each time this patch passes in front of the probe, a trigger signal was generated and converted into a TTL square wave by a National Instruments I/O acquisition board. Given the maximum rotational speed of 600 rpm, the resulting maximum DIC sampling rate  $f_s$  was approximately 10 Hz. In addition to triggering the image acquisition, the optical probe also functioned as an encoder for measuring the instantaneous rotational speed. Since the rotational speed increased slowly during the ramp, it was assumed to remain constant over the duration of each revolution.

#### 4. FEA and hammer test

The analyses presented in this section aimed to inform and guide the design of the subsequent rotation test, rather than to obtain a detailed modal characterization of the blisk.

A finite element (FE) analysis was performed to predict the dynamics of the blisk, considering the effects of rotational speed. The FE model nodes corresponding to the portion of the blisk clamped by the upper flange within a 90-mm diameter were constrained in all degrees of freedom. The modal analysis predicts the presence of the seven modes of the first modal family of the blisk in the  $140 \div 155$  Hz range, and it allows to plot the Campbell diagram of the dummy blisk, as shown in Fig. 6.

Additionally, the non-rotating dummy blisk was experimentally tested using hammer impact excitation, while its out-of-plane vibrations were measured by sampling at 50 kHz with a SLDV, as shown in Fig. 7(a). The scanning laser Doppler vibrometer was preferred over traditional sensors such as strain gauges because strain gauges measure strain rather than displacement, which requires additional postprocessing to be compared with the camera's displacement measurements. Moreover, uncertainties in the strain gauge positioning and in the post-processing of the measured data motivated the choice of a more direct means of comparison.

Twelve hammer impact tests were performed to record the vertical displacement at the tip of each blade. During each test, a modal hammer impacted a point at the root of a blade, while the SLDV recorded the response at the tip of the blade. The resulting FRFs, represented in terms of mobility functions, are shown in Fig. 7(b). Six modes – each characterized by distinct amplitude peaks and a  $360^\circ$  phase shift – were identified in the frequency range of 130–160 Hz. The mode with nodal diameter  $ND = 0$  was not clearly observed during hammer tests, possibly due to low excitation at the impact point, which lies in a low-mobility region for that mode.

Comparison with FEA results suggests that the observed modes belong to the first bending modal family, expected in the frequency range of  $140 \div 155$  Hz (see Fig. 6). However, the experimental FRFs reveal a small mistuning effect. Specifically, the mode with four nodal diameters ( $ND = 4$ ) is split into two nearly orthogonal modes at close frequencies, as highlighted in the zoomed view in Fig. 7(c) and confirmed by the stabilization diagram shown in Fig. 8.

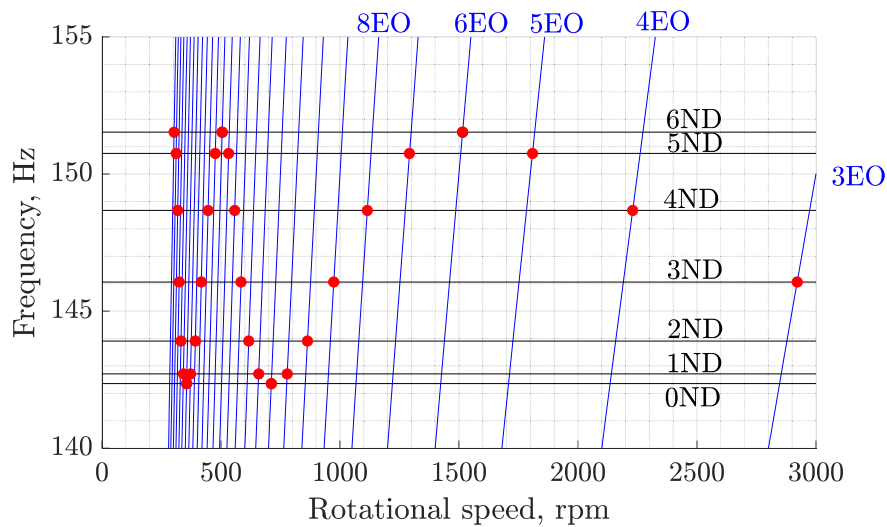


**Fig. 6.** Campbell diagram of the dummy blisk. Green lines represent the frequencies of the modes of the first modal family as a function of rotor speed. Black lines represent the EO excitation frequencies. Red dots indicate resonances.

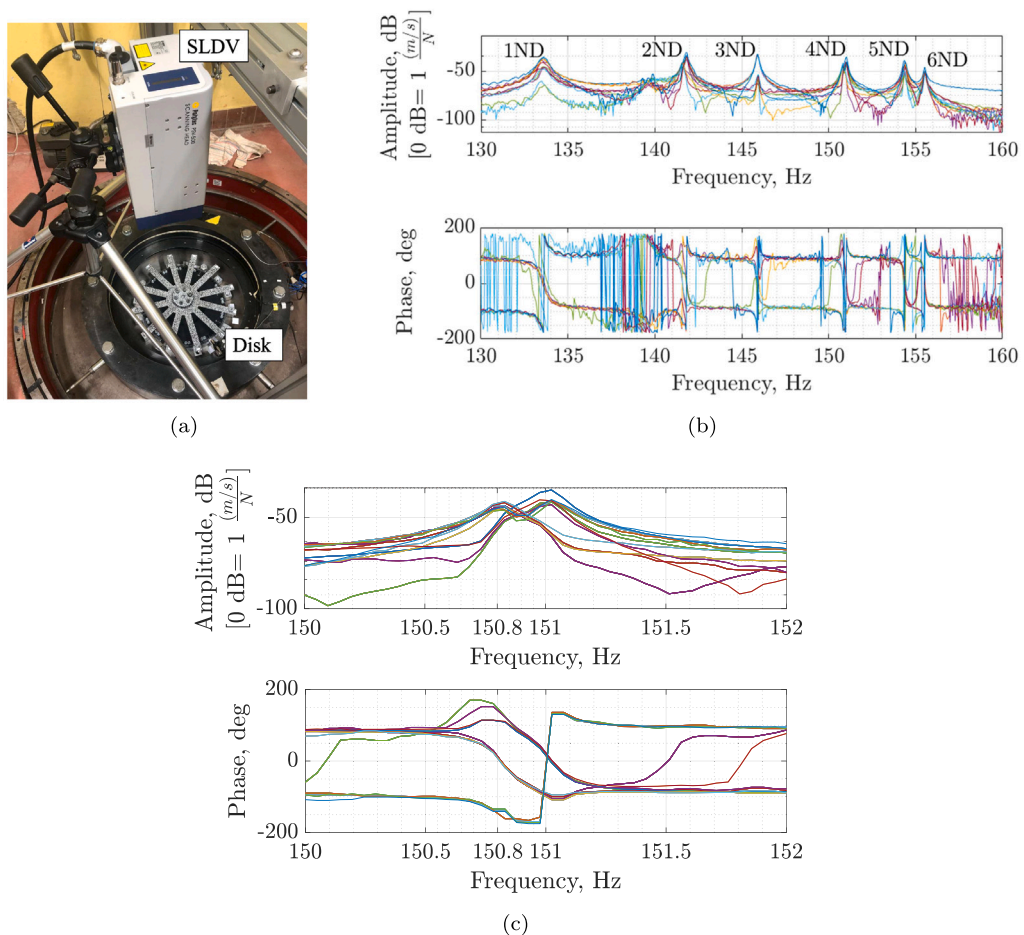


**Fig. 7.** (a) Experimental setup for hammer tests on the non-rotating dummy blisk, (b) corresponding measured FRFs using SLDV, and (c) zoomed view of the FRFs in the frequency range corresponding to the fourth nodal diameter mode. Each color represents the FRF of a different blade.

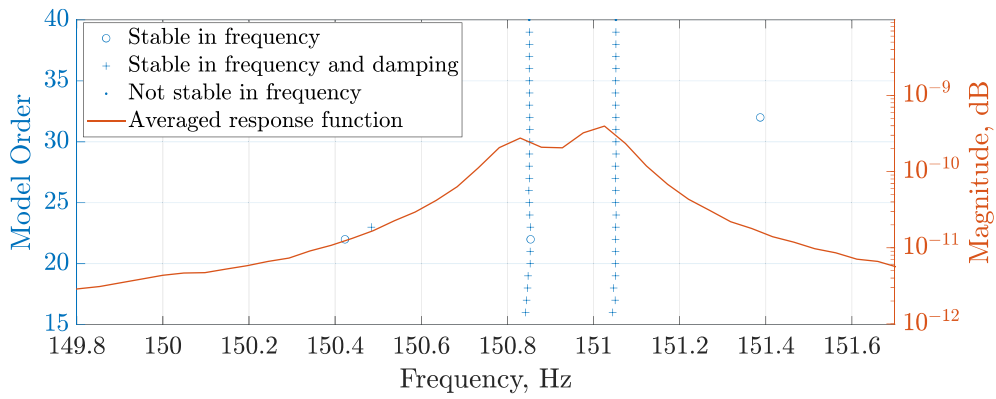


Fig. 8. Stabilization diagram in the frequency range associated with the split modes for  $ND = 4$ .

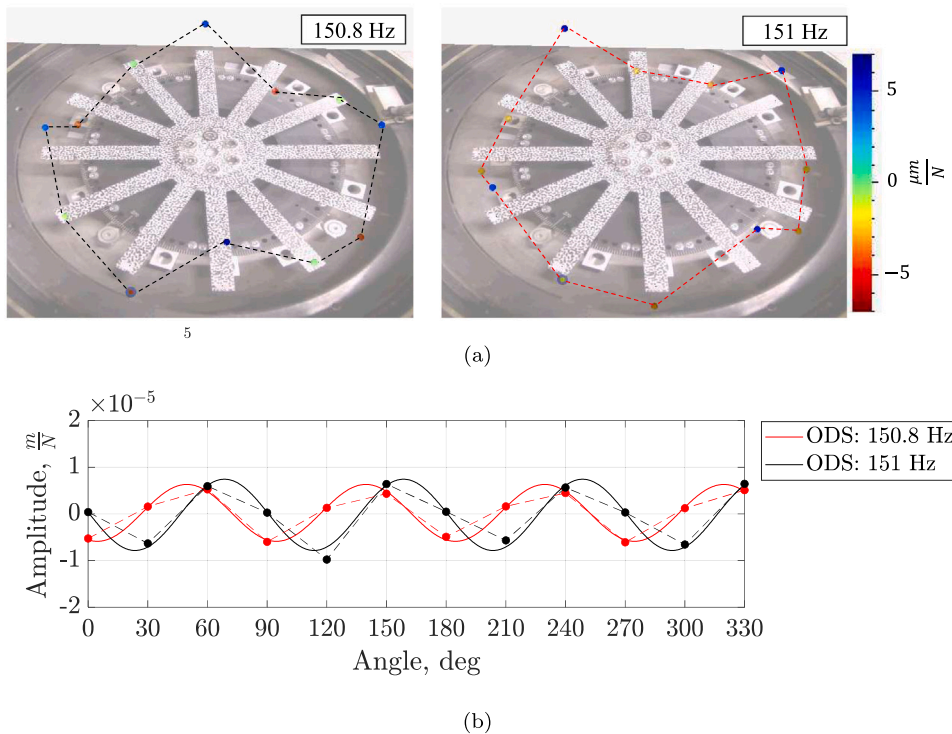


Fig. 9. ODSs measured by SLDV: (a) Experimental ODSs at 150.8 Hz and 151 Hz, extracted from FRFs at the blade tips. (b) Harmonic fitting of the experimental ODSs using a spatial frequency corresponding to  $ND = 4$ . Continuous lines show the fitted curves; dashed lines show the original data.

The stabilization diagram was obtained by processing the experimental FRFs in MATLAB<sup>®</sup> using the Least-Squares Complex Exponential (LSCE) algorithm [34,35]. This algorithm identifies two stable poles at 150.8 Hz and 151.0 Hz, with corresponding modal damping ratios of  $4.46 \cdot 10^{-4}$  and  $4.41 \cdot 10^{-4}$ , respectively. This mode splitting is an effect of mistuning, that the numerical simulation does not capture, because FEM assumes perfect cyclic symmetry. Fig. 9(a) illustrates the ODSs obtained by extracting displacement amplitude and phase for each blade at the two split mode frequencies. To enhance result interpretation, the experimental ODSs – available only at the discrete blade tip locations and shown as dashed lines – were fitted using a harmonic function with a spatial frequency corresponding to four. This harmonic fitting increases the spatial resolution of ODSs, allowing for a clearer visualization of their characteristics. Notably, it reveals that the two split modes are approximately in quadrature. These results are presented in Fig. 9(b), where the dashed lines indicate the experimental data extracted from the FRFs, and the continuous lines represent the fitted harmonic curves.

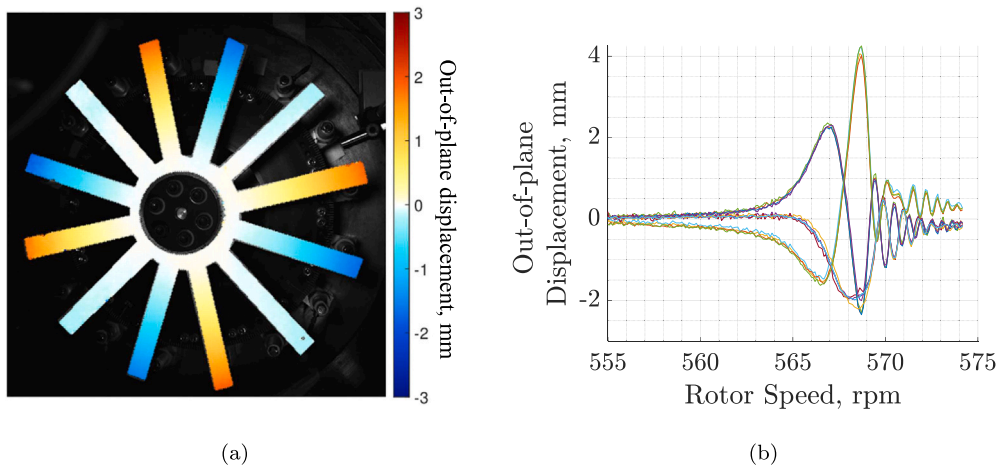


Fig. 10. DIC measurements showing (a) the operational deflection shape (ODS) at reference angle when the blisk rotates at 567 rpm and (b) out-of-plane displacements at the tip of each blade as a function of the blisk speed.

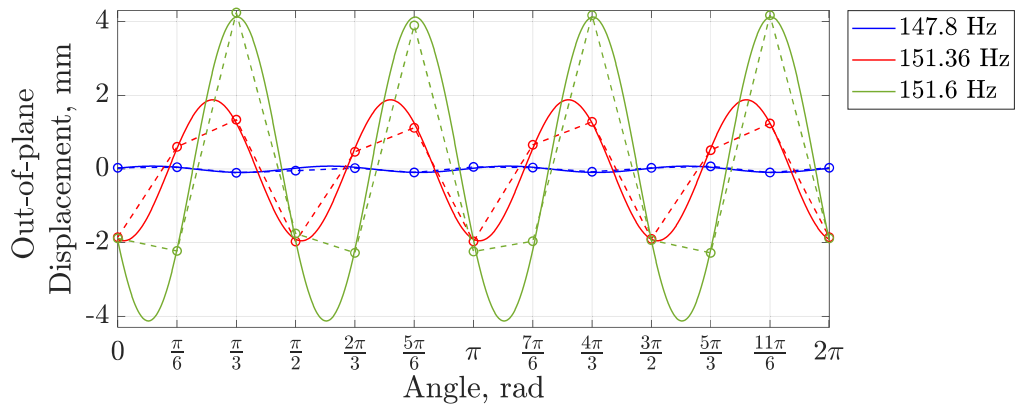


Fig. 11. CHF fitting (continuous lines) of experimental out-of-plane displacement data (dots) acquired at the blade tips at three different rotation speeds corresponding to blade-synchronous vibrations at  $f^* = 147.8$ , 151.36, and 151.6 Hz.

## 5. Results

The DIC system provided downsampled 3D displacement measurements over approximately 27,000 points on the dummy blisk surface. At each measurement time – corresponding to a specific rotational speed – displacement maps were generated. For instance, Fig. 10(a) illustrates the out-of-plane displacement (along the blisk axis) measured at 567 rpm. The spatial distribution confirms the excitation of a mode shape with four nodal diameters ( $ND = 4$ ), consistent with the predicted resonance. As shown in Fig. 10(b), the time histories of the blade tip displacements exhibit pronounced oscillations following peak values, indicating significant transient responses. This behavior suggests that the resonance crossings are rapid enough to produce vibration beating, where the synchronous (steady-state) response coexists with a decaying transient component [8]. As detailed in [36], this effect becomes more prominent with increasing sweep rates.

As can be seen from the peak displacement signals, direct modal identification is prevented due to aliasing. However, the CHF method enables the extraction of modal information despite this limitation. For each excitation frequency  $f^*$ , as defined in Eq. (1), the displacement values  $w(f^*, \theta_i)$  at the  $i$ th blade tip – located at angular positions  $\theta_i$  – are used to solve the overdetermined system in Eq. (7). Fig. 11 presents the results of fitting the experimental blade-tip displacement data (dots) recorded at rotational speeds of  $\Omega^* = 554.3$ , 567.6, and 568.5 rpm using a spatial harmonic function with  $ND = 4$ . These speeds correspond to blade synchronous vibration frequencies of  $f^* = 147.8$ , 151.36, and 151.6 Hz, respectively.

By repeating the CHF procedure across all rotational speeds, the evolution of both amplitude and phase of the ODSs as functions of excitation frequency can be obtained (see Fig. 12). While the amplitude trend shows two peaks, the non-uniform excitation force complicates interpretation. Indeed, the magnetic excitation force depends on the gap between fixed and rotating magnets, which

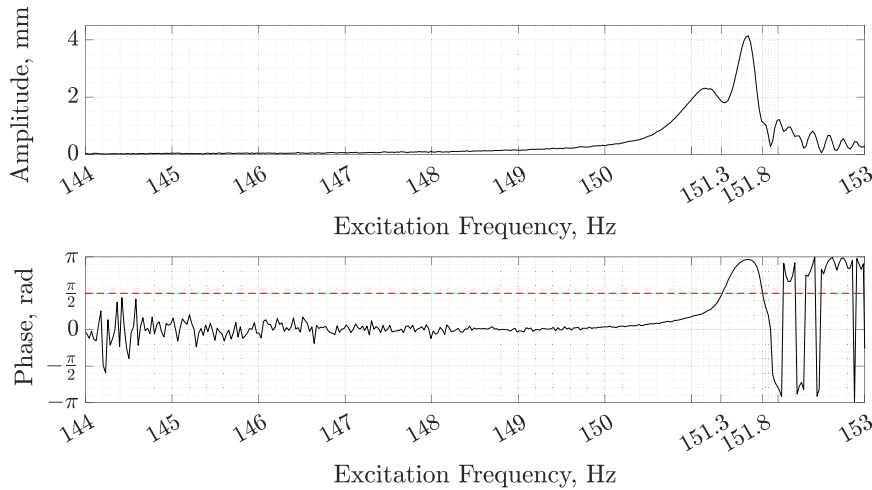


Fig. 12. ODS amplitude and phase evolution obtained from CHF method as functions of excitation frequency.

varies with blade deflection amplitude. Since this force scales inversely with the square of the gap, significant variation occurs near resonance, making amplitude plot unreliable for accurately detecting modal parameters.

In contrast, the phase trend gives information on resonance crossing. A characteristic phase shift of  $\pi/2$  indicates the occurrence of resonance. While, below 147 Hz, phase data are noisy due to low vibration amplitudes, and above 152 Hz the response is affected by transient beating, two resonance frequencies are identified at 151.3 Hz and 151.8 Hz. The corresponding ODSs are illustrated in Fig. 13(a), which shows the out-of-plane displacement maps recorded at 567.6 rpm and 569.2 rpm, i.e. near resonance. Blade tip displacements (dots) are extracted and fitted with a spatial harmonic of  $ND = 4$  (lines) to enhance visualization. As shown in Fig. 13(b), the two ODSs are approximately in quadrature, clearly demonstrating the mode-splitting effect.

As further verification, the Discrete Fourier Transform of the ODSs at the resonance frequencies is plotted in Fig. 13(c), confirming that the excited mode is characterized by a nodal diameter of four. Other spectral components can be attributed to small mistuning effects and measurement noise.

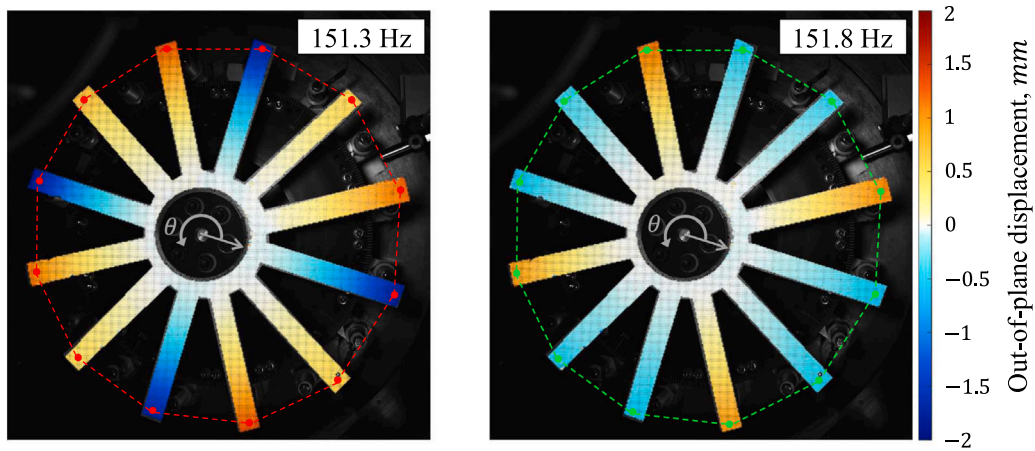
Besides the deformed shape of the blisk, the performed DIC test also provides the 3D point cloud of the object. This information can be exploited to verify the triggering procedure: in principle, since a trigger is used to acquire frames always at the same angular position, the rigid motion of the blisk should be zero. On the other hand, due to experimental issues such as potential inaccuracies in the triggering procedure and vibration of the whole test bench, some discrepancies could be found in the measurements. To assess the extent of this inaccuracy, the first point cloud was set as a reference, and the best-fit rigid body transformation to align all the subsequent point clouds was computed by using the function contained in Caltech's camera calibration toolbox [37]. This function requires as input two point clouds (composed of corresponding points), and provides as output six scalars to define the 3D roto-translation, i.e. three rotation angles and three translation values along the three main axes. The angles were computed in degrees, while the translations were computed in millimeters. Finally, the norm of the three-component vectors was computed to give a metric of total deviation with respect to the theoretical condition of no motion. These values were plotted against the excitation frequency in Fig. 14.

Fig. 14 highlights that in the low frequency range (i.e. about  $144 \div 147$  Hz) there is no relevant vibration of the test bench. On the other hand, a significant increase in vibration amplitude is observed near the resonance region, e.g. between 151 and 152 Hz. Moreover, a noticeable vibration region appears between 147 and 150 Hz, which is attributed to a loss of triggering caused by external vibrations affecting the optical probes. Nevertheless, the amplitudes of the deviations were found to be less than 0.5 degrees for the rotations, and less than 1 mm for the translations, and were considered negligible, thus demonstrating the reliability of the proposed testing procedure.

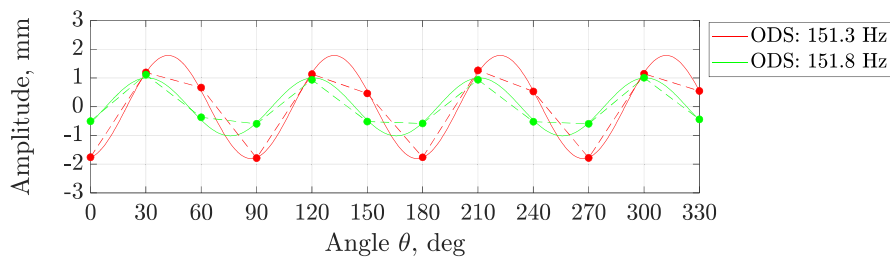
The experimentally determined resonance frequencies for the two orthogonal  $ND = 4$  modes of the dummy blisk are summarized in Table 1. A slight shift in resonance frequency was observed between the stationary and rotating tests, which is attributed to centrifugal stiffening effects.

## 6. Conclusion

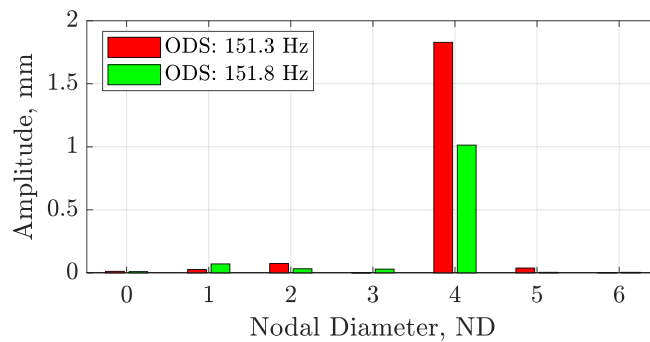
This paper has presented a methodology for using Digital Image Correlation (DIC) with low-speed cameras to experimentally analyze the dynamics of rotating blisks. The proposed approach overcomes limitations of traditional sensors, such as challenges in data transmission and the influence of added sensor mass, while enabling the simultaneous measurement of thousands of points across the blisk surface, capabilities unique to those offered by image-based techniques. Moreover, this methodology is designed to overcome the traditional limitations of DIC in rotor applications, such as decorrelation due to large displacements and the need for



(a) Full field ODSs.



(b) Harmonic fitting of the experimental ODSs extracted at blade tips using a spatial frequency corresponding to  $ND = 4$ . Continuous lines show the fitted curves; dashed lines show the original data.



(c) Amplitude spectrum of ODSs extracted at blade tips.

Fig. 13. ODSs measured by DIC as the blisk rotates at 151.3 Hz and 151.8 Hz.

Table 1

Resonance frequencies of the two orthogonal modes with  $ND = 4$  of the first modal family, identified experimentally from non-rotating (SLDV) and rotating (CHF) tests.

Resonance frequency	Non-rotating test SLDV	Rotating test CHF
$f_{n,1}$ (Hz)	150.8	151.3
$f_{n,2}$ (Hz)	151.0	151.8

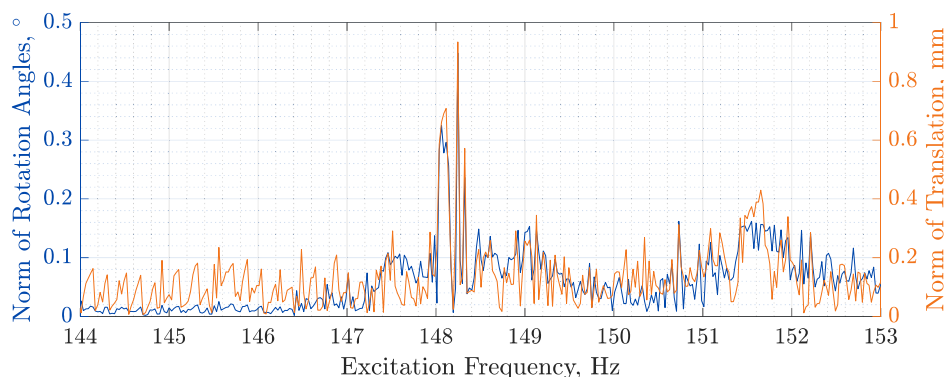


Fig. 14. Estimation of the test bench vibration during operation: comparison between rotational and translational vibrations.

expensive high-speed cameras. By acquiring images at a fixed angular position, the approach eliminates decorrelation issues and enables the use of standard DIC software. This acquisition strategy also reduces sensitivity to lighting variations, as only one image is required per revolution. From the camera's perspective, the disk therefore appears stationary, which minimizes the influence of uneven lighting or shadows. In contrast, when images are acquired at varying angular positions, differences in shading and reflections can lead to decorrelation and reduced measurement accuracy. Thus, the proposed methodology allows tracking the evolution of the phase and amplitude of the ODSs as a function of the excitation frequency, which increases linearly but can be assumed to be constant over each revolution. By analyzing these plots, it is possible to identify resonance conditions and extract the corresponding ODSs. However, only rotating modes can be analyzed, while the maximum amplitudes of stationary modes,  $ND = 0$  and  $ND = N/2$ , cannot be captured.

The proposed approach was experimentally validated on a simplified test article: a dummy blisk with a flat geometry mounted on a dedicated rotation rig. Blade tip displacement signals were extracted and used to identify resonance frequencies. To this end, the Circumferential Harmonic Fit (CHF) method was developed and applied to the DIC data. DIC measurements enabled visualization of high-resolution Operational Distortion Shapes (ODSs) during resonance crossing, including the two orthogonal shapes associated with the  $ND = 4$  mode. This represents a significant advantage, as the method simultaneously tracks a large number of surface points, which would be impractical with traditional point-based sensors.

Although downsampling-based methods generally cannot capture the entire spectrum, this limitation can be mitigated when only a limited frequency band is of interest. In such cases, the frequency information can be concentrated within this band, allowing accurate spectral measurement despite downsampling. This concept represents a potential direction for future development of the method. The proposed method has been shown to be effective in identifying resonance frequencies in the presence of mistuning. However, it does not work properly when the mistuning is large enough to completely destroy the cyclic symmetry.

From a practical standpoint, the maximum measurable angular velocity is limited by the maximum frame rate of the camera. When recording one image per revolution, the sampling rate is equal to the rotation rate; therefore, the maximum measurable rotation rate corresponds to the maximum frame rate of the camera. For standard industrial cameras (such as those used in this study) with frame rates of about 100 fps, this translates to a maximum measurable rotation frequency of approximately 6000 rpm. In practice, such speeds are rarely achievable in air-operated systems, and standard cameras are generally unsuitable for vacuum operation, making frame rate a secondary limitation. A more critical factor is exposure time: at high angular speeds, obtaining sharp, blur-free images becomes difficult. This limitation depends on the minimum exposure time achievable by the camera and the intensity of the available lighting.

#### CRedit authorship contribution statement

**Serena Occhipinti:** Writing – original draft, Software, Methodology, Investigation, Conceptualization. **Alessandra Cesaretti:** Investigation, Data curation. **Christian M. Firrone:** Conceptualization. **Paolo Neri:** Writing – review & editing, Validation, Supervision, Conceptualization. **Daniele Botto:** Writing – review & editing, Supervision, Methodology, Formal analysis, Conceptualization.

#### Declaration of Generative AI and AI-assisted technologies in the writing process

During the preparation of this work the authors used Chat-GPT in order to improve language and readability. After using this tool/service, the authors reviewed and edited the content as needed and takes full responsibility for the content of the publication.

#### Declaration of competing interest

The authors declare that they have no known competing financial interests or personal relationships that could have appeared to influence the work reported in this paper.

## Appendix

A harmonic force  $F(t)$ , whose engine order  $EO$  coincides with a nodal diameter  $ND$ , and is sampled at a frequency  $f_s$  yields the sequence of sample values

$$F^{ND}[n] = F_0 \cos(2\pi ND \frac{\Omega}{60} \frac{n}{f_s} + \varphi) = F_0 \cos(2\pi f_{ND} \frac{n}{f_s} + \varphi) \quad (\text{A.1})$$

while a harmonic force generated by a generic engine order  $EO$  sampled at the same frequency  $f_s$  gives the sequence

$$F^{EO}[n] = F_0 \cos(2\pi EO \frac{\Omega}{60} \frac{n}{f_s} + \varphi) = F_0 \cos(2\pi f_{EO} \frac{n}{f_s} + \varphi) \quad (\text{A.2})$$

For a periodic structure the sampling frequency is driven by the number blades, or sectors more in general,  $N$

$$f_s = \frac{\Omega}{60} N \quad (\text{A.3})$$

If the two frequencies,  $f_{ND}$  and  $f_{EO}$ , are aliases of each other for some integer  $z$

$$f_{EO} = f_{ND} + z f_s \quad (\text{A.4})$$

they will produce identical samples:  $F^{EO}[n] = F^{ND}[n]$  for all  $n$ . The assumption can be easily demonstrated:

$$\begin{aligned} \cos(2\pi f_{EO} \frac{n}{f_s} + \varphi) &= \cos(2\pi (f_{ND} + z f_s) \frac{n}{f_s} + \varphi) \\ &= \cos(2\pi f_{ND} \frac{n}{f_s} + 2\pi z n + \varphi) \\ &= \cos(2\pi f_{ND} \frac{n}{f_s} + \varphi) \end{aligned} \quad (\text{A.5})$$

Then the excitation forces at the two frequencies are  $f_{ND}$  and  $f_{EO}$  are equivalent if Eq. (A.4) holds

$$EO \frac{\Omega}{60} = ND \frac{\Omega}{60} + z N \frac{\Omega}{60} \quad (\text{A.6})$$

Since also negative frequency are possible (A.4) provides the well-known formula

$$EO = zN \pm ND \quad (\text{A.7})$$

## Data availability

Data will be made available on request.

## References

- [1] C. Pierre, Mode localization and eigenvalue loci veering phenomena in disordered structures, *J. Sound Vib.* 126 (3) (1988) 485–502, [http://dx.doi.org/10.1016/0022-460x\(88\)90226-x](http://dx.doi.org/10.1016/0022-460x(88)90226-x).
- [2] M.P. Castanier, C. Pierre, Modeling and analysis of mistuned bladed disk vibration: Current status and emerging directions, *J. Propuls. Power* 22 (2) (2006) 384–396, <http://dx.doi.org/10.2514/1.16345>.
- [3] W. Long, Y. Chen, Reduced order modeling and mistuning identification method for rotating bladed disks under varying speeds, *J. Sound Vib.* 595 (2025) 118687, <http://dx.doi.org/10.1016/j.jsv.2024.118687>.
- [4] L.M. Amoo, On the design and structural analysis of jet engine fan blade structures, *Prog. Aerosp. Sci.* 60 (2013) 1–11, <http://dx.doi.org/10.1016/j.paerosci.2012.08.002>.
- [5] M. Zielinski, G. Ziller, Noncontact vibration measurements on compressor rotor blades, *Meas. Sci. Technol.* 11 (7) (2000) 847–856, <http://dx.doi.org/10.1088/0957-0233/11/7/301>.
- [6] I. Zablotkiy, Y. Korostelev, Measurement of Resonance Vibrations of Turbine Blades with the ELURA Device, Technical Report, Foreign Technology Division, Wright-Patterson AFB, Dayton, OH, USA, 1978.
- [7] G. Schlagwein, U. Schaber, Non-contact blade vibration measurement analysis using a multi-degree-of-freedom model, *Proc. Inst. Mech. Eng. Part A: J. Power Energy* 220 (6) (2006) 611–618, <http://dx.doi.org/10.1243/09576509jpe245>.
- [8] S. Bornassi, T. Berruti, C. Fironne, G. Battiatto, Vibration parameters identification of turbomachinery rotor blades under transient condition using blade tip-timing measurements, *Measurement* 183 (2021) 109861, <http://dx.doi.org/10.1016/j.measurement.2021.109861>.
- [9] Z. Liu, F. Duan, G. Niu, L. Ma, J. Jiang, X. Fu, An improved circumferential Fourier fit (CFF) method for blade tip timing measurements, *Appl. Sci.* 10 (11) (2020) 3675, <http://dx.doi.org/10.3390/app10113675>.
- [10] G. Battiatto, C. Fironne, T. Berruti, Forced response of rotating bladed disks: Blade tip-timing measurements, *Mech. Syst. Signal Process.* 85 (2017) 912–926, <http://dx.doi.org/10.1016/j.ymsp.2016.09.019>.
- [11] D. Di Maio, D. Ewins, Applications of continuous tracking SLDV measurement methods to axially symmetric rotating structures using different excitation methods, *Mech. Syst. Signal Process.* 24 (8) (2010) 3013–3036, <http://dx.doi.org/10.1016/j.ymsp.2010.06.012>.
- [12] L. Lyu, G. Higgins, W. Zhu, Operational modal analysis of a rotating structure using image-based tracking continuously scanning laser Doppler vibrometry via a novel edge detection method, *J. Sound Vib.* 525 (2022) 116797, <http://dx.doi.org/10.1016/j.jsv.2022.116797>.
- [13] S. Boedecker, A. Dräbenstedt, L. Heller, A. Kraft, A. Leonhardt, C. Pape, S. Ristau, E. Reithmeier, C. Rembe, Optical derotator for scanning vibrometer measurements on rotating objects, in: Seventh International Conference on Vibration Measurements By Laser Techniques: Advances and Applications, 6345, SPIE, 2006, p. 63450M, <http://dx.doi.org/10.1117/12.693066>.
- [14] R.A. Lomenzo, A.J. Barker, A.L. Wicks, Laser vibrometry system for rotating bladed disks, in: Proceedings of the 18th IMAC, 1999, pp. 277–282.

- [15] D. Minervini, D. Mastrodicasa, T. Geluk, E. Di Lorenzo, Novel methodology for isolating rotational phenomena in tire testing, *INTER-NOISE NOISE-CON Congr. Conf. Proc.* 268 (7) (2023) 1845–1856.
- [16] R. Hunady, P. Pavelka, P. Lengvarský, Vibration and modal analysis of a rotating disc using high-speed 3D digital image correlation, *Mech. Syst. Signal Process.* 121 (2019) 201–214, <http://dx.doi.org/10.1016/j.ymssp.2018.11.024>.
- [17] S. Occhipinti, D. Mastrodicasa, S. Manzato, E. Di Lorenzo, Application of digital image correlation in operational modal analysis of rotating structures, in: *ISMA 2024 Conference Proceedings*, 2024, p. 2544.
- [18] L. Wang, S. Bi, H. Li, Y. Gu, C. Zhai, Fast initial value estimation in digital image correlation for large rotation measurement, *Opt. Lasers Eng.* 127 (2020) 105838, <http://dx.doi.org/10.1016/j.optlaseng.2019.105838>.
- [19] R. Wu, H. Qian, D. Zhang, Robust full-field measurement considering rotation using digital image correlation, *Meas. Sci. Technol.* 27 (10) (2016) 105002, <http://dx.doi.org/10.1088/0957-0233/27/10/105002>.
- [20] S. Barone, P. Neri, A. Paoli, A.V. Razonale, Low-frame-rate single camera system for 3D full-field high-frequency vibration measurements, *Mech Syst Signal Pr* 123 (2019) 143–152, <http://dx.doi.org/10.1016/j.ymssp.2019.01.016>.
- [21] Y. Kato, S. Watahiki, Vibration mode identification method for structures using image correlation and compressed sensing, *Mech. Syst. Signal Process.* 199 (2023) 110495, <http://dx.doi.org/10.1016/j.ymssp.2023.110495>.
- [22] M. Rani, S.B. Dhok, R.B. Deshmukh, A systematic review of compressive sensing: Concepts, implementations and applications, *IEEE Access* 6 (2018) 4875–4894, <http://dx.doi.org/10.1109/ACCESS.2018.2793851>.
- [23] D. Botto, S. Occhipinti, C.M. Firrone, P. Neri, High-frequency nonlinear vibration analysis through low-frequency stereo-camera systems, *Mech. Syst. Signal Process.* 223 (2025) 111821, <http://dx.doi.org/10.1016/j.ymssp.2024.111821>.
- [24] Y. Wang, F.S. Egner, T. Willems, M. Kirchner, W. Desmet, Camera-based experimental modal analysis with impact excitation: Reaching high frequencies thanks to one accelerometer and random sampling in time, *Mech. Syst. Signal Process.* 170 (2022) 108879, <http://dx.doi.org/10.1016/j.ymssp.2022.108879>.
- [25] Y.L. Dong, B. Pan, A review of speckle pattern fabrication and assessment for digital image correlation, *Exp. Mech.* 57 (8) (2017) 1161–1181, <http://dx.doi.org/10.1007/s11340-017-0283-1>.
- [26] K. Zaletelj, V. Agrež, J. Slavič, R. Petkovšek, M. Boltežar, Laser-light speckle formation for deflection-shape identification using digital image correlation, *Mech. Syst. Signal Process.* 161 (2021) 107899, <http://dx.doi.org/10.1016/j.ymssp.2021.107899>.
- [27] A. Sinha, *Vibration of Nearly Periodic Structures and Mistuned Bladed Rotors*, Cambridge University Press, Cambridge, United Kingdom, 2017, Includes bibliographical references (pages 179-184) and index.
- [28] R. Hartley, A. Zisserman, *Multiple View Geometry in Computer Vision*, Cambridge University Press, 2004, <http://dx.doi.org/10.1017/cbo9780511811685>.
- [29] T.M. Inc., *Computer vision toolbox*, 2023, URL: <https://www.mathworks.com>.
- [30] J. Blaber, B. Adair, A. Antoniou, Ncorr: Open-source 2D digital image correlation matlab software, *Exp. Mech.* 55 (6) (2015) 1105–1122, <http://dx.doi.org/10.1007/s11340-015-0009-1>.
- [31] G. Battiatto, *Vibrations Prediction and Measurement of Multi-Stage Bladed Disks with Non Linear Behavior Due to Friction Contacts* (Ph.D. thesis), Politecnico di Torino, 2017, <http://dx.doi.org/10.6092/POLITO/PORTO/2680969>.
- [32] D.H. Diamond, P.S. Heyns, A.J. Oberholster, A comparison between three blade tip timing algorithms for estimating synchronous turbomachine blade vibration, in: *9th WCEAM Research Papers*, Springer International Publishing, 2015, pp. 215–225, [http://dx.doi.org/10.1007/978-3-319-15536-4\\_18](http://dx.doi.org/10.1007/978-3-319-15536-4_18).
- [33] L. Carassale, R. Guida, M. Marrè-Brunenghi, Modal identification of bladed disks by time–frequency analysis of the nonsynchronous response, *J. Eng. Gas Turbines Power* 145 (2) (2022) <http://dx.doi.org/10.1115/1.4055684>.
- [34] T. Inc., *System Identification Toolbox*, 2024, URL.
- [35] T. Nestorović, M. Trajkov, M. Patalong, Identification of modal parameters for complex structures by experimental modal analysis approach, *Adv. Mech. Eng.* 8 (5) (2016) <http://dx.doi.org/10.1177/1687814016649110>.
- [36] L. Carassale, M. Marrè-Brunenghi, S. Patrone, Damping estimation for turbine blades under non-stationary rotation speed, in: *Special Topics in Structural Dynamics*, Volume 6, Springer International Publishing, 2015, pp. 145–152.
- [37] J.-Y. Bouguet, *Camera calibration toolbox for matlab*, 2022, <http://dx.doi.org/10.22002/D1.20164>.